RSC Advances

PAPER

View Article Online
View Journal | View Issue

Cite this: *RSC Adv.*, 2017, **7**, 23812

A direct four-electron process on Fe–N_3 doped graphene for the oxygen reduction reaction: a theoretical perspective†

Xiaowan Bai,[ac] Erjun Zhao,*[a] Wencheng Wang,*[b] Ying Wang,[c] Kai Li,[c] Lin Lin,[a] Jucai Yang,[d] He Sun[e] and Zhijian Wu*[c]

As one of the potential candidates for electrocatalysis, non-precious transition metal and nitrogen co-doped graphene has attracted extensive attention in recent years. A deep understanding of the oxygen reduction reaction (ORR) mechanism including the specific active sites and reaction pathways will contribute to the further enhancement of the catalytic activity. In this study, the reaction mechanism for ORR on Fe–N_3 doped graphene (Fe–N_3-Gra) is investigated theoretically. Our results show that Fe–N_3-Gra is thermodynamically stable. The ORR elementary reactions take place within a small region around the Fe–N_3 moiety and its adjacent six C atoms. HOOH does not exist on the catalyst surface, indicating a direct four-electron process for Fe–N_3-Gra. The kinetically most favorable pathway is O_2 hydrogenation, in which the formation of the second H_2O is the rate-determining step with an energy barrier of 0.87 eV. This value is close to 0.80 eV for pure Pt, suggesting that Fe–N_3-Gra could be a potential electrocatalyst. Free energy changes at different electrode potentials are also discussed.

Received 17th March 2017
Accepted 24th April 2017

DOI: 10.1039/c7ra03157b

rsc.li/rsc-advances

1. Introduction

Fuel cells (FCs) have attracted worldwide attention because of their high energy conversion efficiency, high power density, and low emission.[1] The electrochemical performance of a fuel cell largely relies on the oxygen reduction reaction (ORR) at the cathode which determines the efficiencies of the energy conversion and storage. The ORR is, however, sluggish and thus a highly efficient cathode catalyst is required.[2,3] Up to now, the most effective cathode catalysts for the ORR have been the Pt-based catalysts.[4–6] Nonetheless, their large-scale commercial applications are limited by high cost, poor CO tolerance, and low durability and stability.[7] Therefore, alternative materials that are earth-abundant, cost-effective and have high catalytic activities comparable to or higher than those of Pt-based catalysts are in demand. In this aspect, the pioneering work was done by Jasinski in 1964, which reported that the cobalt phthalocyanine could be used as catalyst for oxygen reduction.[8] Based on this idea, in recent years, the transition metal-coordinated (*e.g.*, Fe, Co and Mn) nitrogen-doped carbon matrix (M–N_x–C) electrocatalysts for the ORR have been studied extensively as promising alternatives to Pt-based catalysts in experiments.[9–18] The non-precious metal catalysts derived from polyaniline, iron, and cobalt show high catalytic activity with remarkable performance and stability as well as excellent four-electron selectivity (hydrogen peroxide yield <1.0%).[9] The current density of the cathode made with the microporous Fe–N_x–C catalyst could be equal to that of a Pt-based cathode at a cell voltage of larger than 0.9 V.[10] The Co–N_x co-doped graphene has comparable ORR performance to the commercial Pt–C electrocatalysts.[13] The Mn-doped glycine-derived carbon catalyst has a high catalytic activity for the ORR and low half-wave potential than that of commercial Pt–C.[17] Furthermore, theoretical studies have been also available for M–N_x–C electrocatalysts for the ORR[19–23] and these studies revealed that they possess high catalytic activity for the ORR.

Among the M–N_x–C catalytic systems, Fe–N_x–C electrocatalysts are studied most both experimentally[9–12,18,24–27] and theoretically.[19,20,28–32] In-depth structure-to-property relation

[a]*College of Science, Inner Mongolia Key Laboratory of Theoretical Chemistry Simulation, Inner Mongolia University of Technology, Hohhot 010051, P. R. China. E-mail: ejzhao@yahoo.com*

[b]*Radiotherapy Laboratory, Jilin Cancer Hospital, Changchun 130012, P. R. China. E-mail: wencheng.w@163.com*

[c]*State Key Laboratory of Rare Earth Resource Utilization, Changchun Institute of Applied Chemistry, Chinese Academy of Sciences, Changchun 130022, P. R. China. E-mail: zjwu@ciac.ac.cn*

[d]*School of Energy and Power Engineering, Inner Mongolia University of Technology, Hohhot 010051, P. R. China*

[e]*The Computing Center of Jilin Province, Changchun 130012, P. R. China*

† Electronic supplementary information (ESI) available: Fig. S1 is possible configurations for each adsorbed species (side-on O_2, end-on O_2, O + O, O, OH, OOH, O + OH, OH + OH, H_2O and H) involved in the ORR on the Fe–N_3 embedded in graphene (Fe–N_3-Gra). Fig. S2 is O hydrogenation into OH (d_1). Fig. S3 is the HOOH decomposed process with time. See DOI: 10.1039/c7ra03157b

presents an evidence that Fe–N_x centers are the active sites playing a key role in oxygen reduction reaction.[11] Indeed, Fe–N_4 moiety as the catalytic active site was observed by diverse experimental studies.[24,33,34] The atomic structure of highly active Fe–N_4-Gra has been analyzed by X-ray absorption spectroscopy[24] and high-resolution transmission electron microscopy.[35] The current density of ORR to the number of in-plane Fe–N_4 centers was identified using Mössbauer spectra.[33] Theoretical studies also confirmed that Fe–N_4 doped graphene has high catalytic activity for ORR comparable to that of Pt catalyst with Fe–N_4 moiety as active sites.[19,20,31] The most favorable reaction pathway for Fe–N_4 doped graphene is a four-electron OOH dissociation process.[20] Besides Fe–N_4, Fe–N_3 doped carbon matrix has been also studied for ORR in the pyrolyzed catalyst.[11,12] The experimental study suggests that the Fe–N_3 doped graphene also exhibits high ORR activity, high stability, and low H_2O_2 production.[36] Theoretical studies revealed that the Fe–N_3 doped graphene is thermodynamically stable with the negative formation energy.[30,37] Clustered Fe–N_3 structures can cleave the O–O bond very easily.[29] However, up to date, the catalytic activity and the detailed mechanism for ORR remain unclear for Fe–N_3–C catalysts. In particular, for Fe–N_4 doped graphene, direct four-electron process is observed for ORR both experimentally[12] and theoretically.[20] For Fe–N_3 doped graphene, however, it is not clear whether it catalyzes the four-electron direct reduction of O_2 molecule to water or also catalyzes the second step HOOH reduction to water through a two-electron process.[12] Therefore, it is highly necessary to unravel the physical insights of Fe–N_3 doped graphene from the atomic and electronic point of view. To achieve this goal, the catalytic active sites and the reaction pathways for Fe–N_3 doped graphene have been studied by using the density functional theory (DFT) in this work.

2. Computational details

2.1 Methods

All spin-polarized DFT[38,39] calculations were performed using the Vienna ab initio simulation package (VASP).[40,41] The interactions between valence electrons and frozen cores were described by the projector augmented wave (PAW) method.[42] The electronic exchange–correlation energy was treated by the generalized gradient approximation of the Perdew–Burke–Ernzerhof (PBE) functional.[43] The kinetic energy cutoff was set to be 400 eV for the plane-wave expansion. A 5 × 5 × 1 Monkhorst–Pack grid was used to provide sufficient accuracy in the integration of the Brillouin zone.[44] The transition state (TS) searches were performed by employing the climbing image nudged elastic band (CI-NEB) method,[45] and was confirmed by only one imaginary frequency on the potential energy surface. For geometry optimizations and TS searches, the convergence tolerances of the electronic and ionic iterations were set to 10^{-5} eV and 0.05 eV $Å^{-1}$, respectively. The van-der-Waals (vdW) interactions were considered by using the semiempirical scheme proposed by DFT-D2 method of Grimme[46,47] in all of the calculations.

Free energy calculation of each elementary reaction on the Fe–N_3-Gra surface was performed based on computational hydrogen electrode (CHE) model suggested by Nørskov *et al.*[48] The computational detail of the free energy change (ΔG) is as follows:

$$\Delta G = \Delta E + \Delta \mathrm{ZPE} - T\Delta S + \Delta G_{\mathrm{pH}} + \Delta G_{\mathrm{U}} \quad (1)$$

where ΔE is the reaction energy obtained from DFT calculations, ΔZPE is the zero point energy correction, T is the temperature (298.15 K), and ΔS is the entropy change. ΔG_{pH} is the correction of H^+ free energy by the concentration, $\Delta G_{\mathrm{pH}} = k_{\mathrm{B}}T \times \ln 10 \times \mathrm{pH}$, where k_{B} is the Boltzmann constant and T = 300 K. pH = 0 is assumed for acidic medium. $\Delta G_{\mathrm{U}} = -neU$, where n is the number of transferred electrons and U is the electrode potential. In acidic environment, the U values range from 0 to 1.23 V.[48]

2.2 Models

A 5 × 5 hexagonal supercell of graphene (containing 50 atoms) with Fe–N_3 coordinated structure (Fig. 1a) was built based on the experimental studies.[11,12] The lattice parameters were a = b= 12.3 Å, and the graphene sheets were separated by a 15 Å vacuum layer along the c direction to avoid interactions between periodic images. All atoms were allowed to relax during the geometry optimization. To check the stability of Fe–N_3-Gra, the formation energy was calculated as:

$$\Delta E_{\mathrm{f}} = E_{\mathrm{Fe\text{–}N_3\text{-}Gra}} + 4\mu_{\mathrm{C}} - (E_{\mathrm{Gra}} + 3\mu_{\mathrm{N}} + \mu_{\mathrm{Fe}}) \quad (2)$$

where $E_{\mathrm{Fe\text{–}N_3\text{-}Gra}}$ and E_{Gra} are the total energies of Fe–N_3 doped graphene (Fe–N_3-Gra) and the pristine graphene, respectively. μ_{C} is the chemical potential of the carbon atom defined as the total energy per carbon atom in a pristine graphene.[32] μ_{N} is the chemical potential of nitrogen taken as one-half of the total

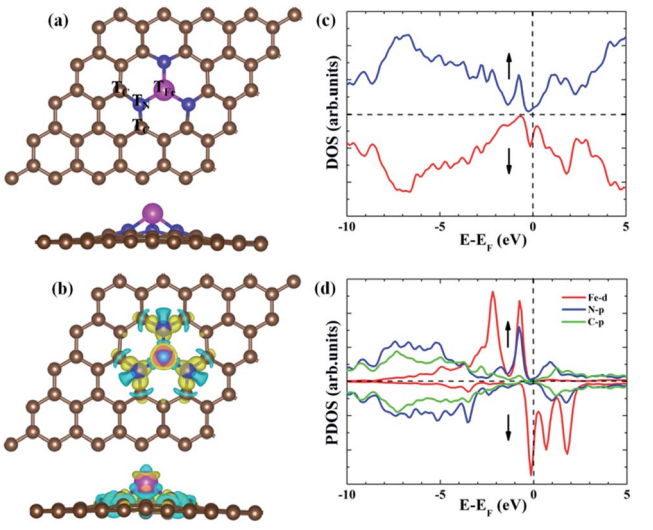

Fig. 1 (a) Possible adsorption sites on the Fe–N_3-Gra involved in the ORR. (b) The differential charge density distribution for Fe–N_3-Gra. Isosurface value = 0.01. The cyan and yellow colors represent charge accumulation and depletion, respectively. (c) The total density of states (DOS) for Fe–N_3-Gra. (d) Partial DOS for Fe–N_3-Gra.

energy of the N_2 molecule in the gas phase.[30,37] μ_{Fe} is computed for an isolated Fe atom.[22,37,49]

The adsorption energy (ΔE_{ads}) was calculated as:

$$\Delta E_{ads} = E_{adsorbate/Fe-N_3-Gra} - (E_{adsorbate} + E_{Fe-N_3-Gra}) \quad (3)$$

where $E_{adsorbate/Fe-N_3-Gra}$, $E_{adsorbate}$ and E_{Fe-N_3-Gra} are the total energies of the Fe–N_3-Gra with adsorbate, the isolated adsorbate, and clean Fe–N_3-Gra, respectively.

3. Results and discussion

3.1 Structure and electronic properties of Fe–N_3-Gra

Compared with the formation energy of −0.95 eV from Kattel *et al.*[37] and −1.0 eV from Kabir *et al.*,[30] our calculated formation energy for Fe–N_3-Gra is −1.66 eV, slightly larger than the previous results due to the different model system and the consideration of the Van der Waals interactions in this work. The electronic density of states (DOS) (Fig. 1c) suggests that Fe atom has a finite density of states at the Fermi energy level, implying the metallic character for Fe–N_3-Gra. The partial density of states (PDOS) shows that there is a strong hybridization between the 2p orbital of N atom and the 3d orbital of Fe atom near the Fermi energy level (−1.5 to 0 eV, Fig. 1d). At the lower energy level (<−1.5 eV), the DOS is mainly contributed by the strong hybridization between the 2p orbital of N atom and the 2p orbital of C atom. These results suggest that the electronic interaction leads to the bond formation of N–Fe and N–C, resulting in lower formation energy for Fe–N_3-Gra, similar to the previous study.[37] Bader charge analysis reveals that Fe atom has positive charge 0.96 |e| for clean Fe–N_3-Gra (Table 1). The three nitrogen atoms are negatively charged by −3.59 |e|. The total charges of the six carbon atoms bonding to the nitrogen atoms are positively charged by 2.45 |e|. These results reveal that due to the different electronegativity of doping atoms and carbon, the local electroneutrality is broken and charge transfer occurs. The small net charge −0.18 |e| between Fe–N_3 moiety and its adjacent six carbon atoms suggests that the small region around Fe–N_3 moiety and its adjacent six carbon atoms can be served as the catalytic active center for ORR on the Fe–N_3-Gra surface. This is in agreement with the charge density difference (Fig. 1b). Hence, the possible adsorption sites for the ORR intermediates are the top sites of the Fe, N and C atoms, namely T_{Fe}, T_N and T_C, as shown in Fig. 1a.

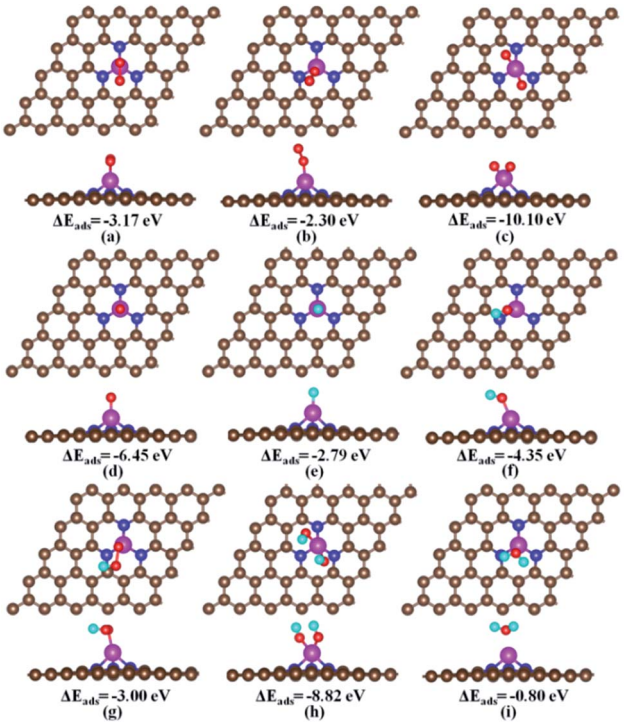

Fig. 2 The most stable adsorption configurations of the ORR intermediates on the Fe–N_3-Gra. ΔE_{ads} is the adsorption energy (eV). (a) Side-on O_2, (b) end-on O_2, (c) two separated O atoms, (d) atomic O, (e) atomic H, (f) OH, (g) OOH, (h) two OH co-adsorption, and (i) H_2O. In the figure, the brown, pink, blue, red, and cyan balls represent C, Fe, N, O and H atoms, respectively.

3.2 Adsorption of the ORR intermediates on the Fe–N_3-Gra

For each ORR intermediate *i.e.*, O_2, O + O, H, O, OH, OOH, HOOH, and H_2O, we optimized its various possible adsorption configurations at different adsorption sites on the Fe–N_3-Gra. The obtained stable adsorption structures and adsorption

Table 1 The Fe–O and O–O bond distance (Å) in FeN_3-Gra and Bader charge (Q [e]). Q(Fe), Q(N_3), Q(C-total) and Q(ads) refer to the total charge on Fe, N_3, the six adjacent C atoms connecting to the three N atoms, and each adsorbate, respectively. NC refers to the net change and is the sum of Q(Fe) + Q(N_3) + Q(C-total) + Q(ads). The values in the brackets are from the solvent environment

	d_{Fe-O}	d_{O-O}	Q(Fe)	Q(N_3)	Q(C-total)	Q(ads)	NC
FeN_3	—	—	0.96	−3.59	2.45	0.00	−0.18
Side-on O_2	1.82(1.83)	1.42(1.44)	1.22	−3.44	2.58	−0.80	−0.44
End-on O_2	1.69(1.70)	1.30(1.34)	1.14	−3.53	2.88	−0.62	−0.13
2O	1.63(1.66)	2.65(2.60)	1.40	−3.43	2.92	−1.23	−0.34
O	1.60(1.62)	—	1.15	−3.42	2.78	−0.65	−0.14
H	—	—	1.07	−3.62	2.97	−0.42	0.00
OH	1.76(1.79)	—	1.15	−3.41	2.39	−0.51	−0.38
OOH	1.84(1.86)	1.49(1.50)	1.25	−3.63	2.61	−0.59	−0.36
2OH	1.82(1.86)	2.67(2.64)	1.38	−3.50	2.72	−1.00	−0.40
H_2O	2.11(2.03)	—	1.06	−3.65	2.89	0.06	0.36

Table 2 Adsorption energies (eV) of the ORR intermediates on Fe–N_3-Gra. The values in the brackets are from the solvent environment. The comparison with other electrocatalysts is also listed

	O_2	O	OH	OOH	H_2O
Fe–N_3	−3.17[g]/−2.30[h]	−6.45	−4.35	−3.00	−0.80
Fe–N_3-sol	(−3.11[g]/−2.32[h])	(−6.35)	(−4.05)	(−2.68)	(−0.83)
Fe–N_3[a]	−2.45	—	—	—	—
Fe–N_2[b]	−1.78	−5.12	−3.25	−2.08	−0.33
Fe–N_4[c]	−0.95	−4.37	−2.94	−1.87	−0.48
Fe–N_4[d]	−0.98	−4.35	−2.80	−1.76	−0.18
Fe-phthalocyanine[e]	−1.16	—	−3.41	—	−1.05
Pt(111)[f]	−0.62	−4.30	−2.21	−0.94	−0.20
Pt(100)[f]	−1.10	−4.38	−2.77	−1.30	−0.25

[a] Ref. 50, doped in carbon nanotube. [b] Ref. 32. [c] Ref. 19. [d] Ref. 20. [e] Ref. 51. [f] Ref. 52. [g] Side-on configuration, this work. [h] End-on configuration, this work.

energies are shown in Fig. S1, ESI.† The most stable adsorption structures and energies are summarized in Fig. 2 and Table 2, respectively.

The favorable adsorption of the O_2 molecule on the Fe–N_3-Gra is the prerequisite for ORR to proceed. For O_2 adsorption, we obtained two adsorption configurations, that is, side-on and end-on. In the side-on configuration (Fig. 2a), the adsorbed O_2 molecule is parallel to the catalyst surface and forms two equal bond distances with Fe atom (Fe–O: 1.82 Å). The adsorption energy of −3.17 eV is stronger than that of −2.45 eV in Fe–N_3 doped carbon nanotube.[50] Upon adsorption, the O–O bond length is elongated to 1.42 Å compared with 1.22 Å in the free gas phase O_2, and the charge transfer from Fe–N_3-Gra to O_2 is −0.80 |e|, which indicates that a chemisorption exists between O_2 and Fe–N_3-Gra. This would facilitate the O_2 dissociation. For the end-on configuration (Fig. 2b), only one O atom bonds to the Fe atom with Fe–O bond distance 1.69 Å, while the other O atom is pointing away from the catalyst surface. Its adsorption energy is −2.30 eV, smaller than −3.17 eV for side-on configuration. The O–O bond length and charge transfer of end-on O_2 are 1.30 Å and −0.62 |e|, respectively. As the final state for O_2 dissociation, the two separated O atoms are co-adsorbed at top Fe site (Fig. 2c) with an energy of −10.10 eV. The charge transfer −1.23 |e| is nearly two times of the single O atom of −0.65 |e|. The adsorption energy of single O atom is −6.45 eV, which is the strongest among the studied single ORR intermediates, similar to the previous studies.[19,20,32]

For hydrogen-containing intermediates (Fig. 2e–g), the most favorable adsorption site of H, OH, and OOH is the top Fe site with the adsorption energies of −2.79 eV, −4.35 eV, and −3.00 eV, respectively. For H atom, the second most favorable adsorption site is on the C atoms adjacent to N atoms with an adsorption energy of −1.50 eV (Fig. S1†). Since the top Fe site is always occupied by O-containing species during the reaction, the C atoms adjacent to N atoms are the primary active site for the adsorption of hydrogen in the hydrogenation reaction. For H_2O, the adsorption energy is −0.80 eV. The charge transfer from Fe–N_3-Gra to H_2O is 0.06 |e| with relatively long Fe–O distance of 2.11 Å (Fig. 2i), indicating that it might be desorbed easily from the Fe–N_3-Gra surface once it is formed.

For the HOOH species, the DFT study shows that it does not exist and is decomposed into either O + H_2O or OH + OH configurations. Quantum Chemical Molecular dynamics study confirmed this point (details concerning the computational method and corresponding results are presented in ESI†). The cleavage of O–O bond is observed at very short time (Fig. 3). Both O + H_2O and OH + OH configurations are observed depending on the different initial parameters. Therefore, the direct four-electron process occurs on the Fe–N_3-Gra surface.

3.3 ORR mechanism on the Fe–N_3-Gra

As mentioned above, the adsorption of O_2 molecule is the first step to initialize the ORR on the catalyst. Upon the O_2 adsorption, the ORR would proceed through two possible reaction pathways, *i.e.*, O_2 dissociation and O_2 hydrogenation, as shown in Fig. 4. We will introduce these reaction pathways in the following.

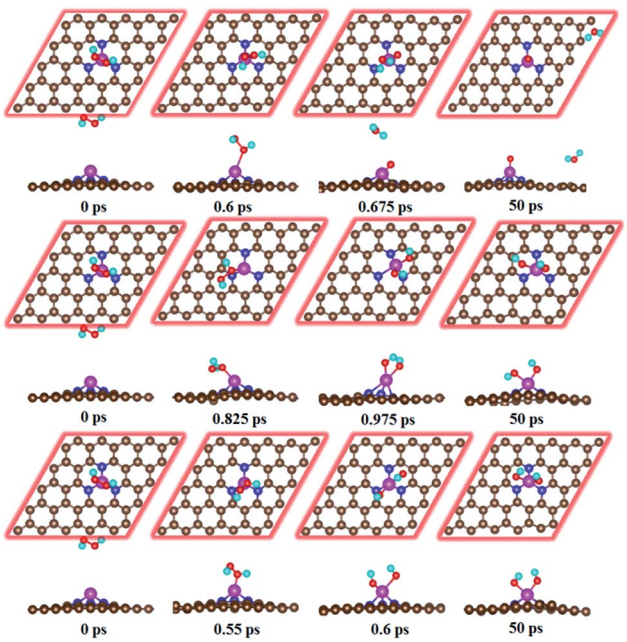

Fig. 3 Evolution of molecular dynamic simulations of the HOOH species without adsorbing (d_{Fe-O} = 5 Å) on the Fe–N_3-Gra surface at 300 K.

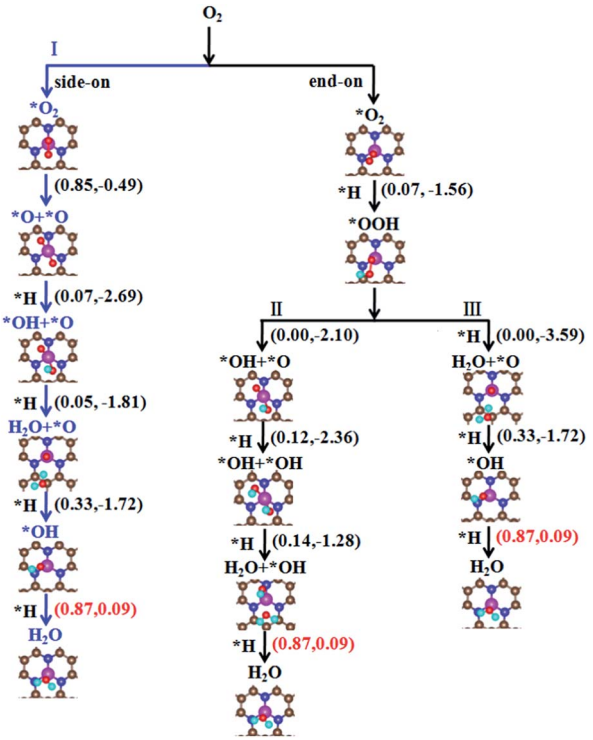

Fig. 4 Possible reaction pathways for ORR on the Fe–N_3-Gra. The numbers in parenthesis are the energy barriers and reaction energies in units of eV. * denotes that the ORR species is adsorbed on the catalyst surface.

O_2 dissociation – pathway I. For end-on configuration with smaller adsorption energy (−2.30 eV), our calculation indicates that it first converges to side-on configuration in searching the transition state of O_2 dissociation. This means that the side-on configuration is the first step in O_2 dissociation. During the reaction, the chemisorbed O_2 molecule undergoes the O–O bond cleavage to form two separated O atoms (Fig. 5a_1). At transition state, the O–O bond is enlarged to 1.80 Å compared with 1.42 Å in the initial state. For final state, the two separated O atoms are co-adsorbed at Fe atom with O–O distance of 2.65 Å. The $O_2 \rightarrow O + O$ reaction is exothermic with an energy of −0.49 eV and costs an energy of 0.85 eV, smaller than 1.19 eV (ref. 20) and 2.53 eV (ref. 19) for the O_2 dissociation in FeN_4 doped graphene. This implies that the O_2 dissociation would be relatively easy on the Fe–N_3-Gra surface. Following the O_2 dissociation, one of the O atoms is first hydrogenated to form O + OH with an energy barrier of 0.07 eV and a large of reaction energy of −2.69 eV as shown in Fig. 5b_1. After the O + OH species is generated, both the single O atom and OH will be hydrogenated. We will first discuss the hydrogenation of OH, while the hydrogenation of single O atom will be discussed in O_2 hydrogenation reaction in the following section. The hydrogenation of OH forms the first H_2O (Fig. 5c_1) with a small energy barrier of 0.05 eV. The $O + OH + H \rightarrow O + H_2O$ reaction is exothermic by −1.81 eV. After the first H_2O molecule is desorbed from the Fe–N_3-Gra surface, the remaining O atom will proceed with two sequential hydrogenation processes to form

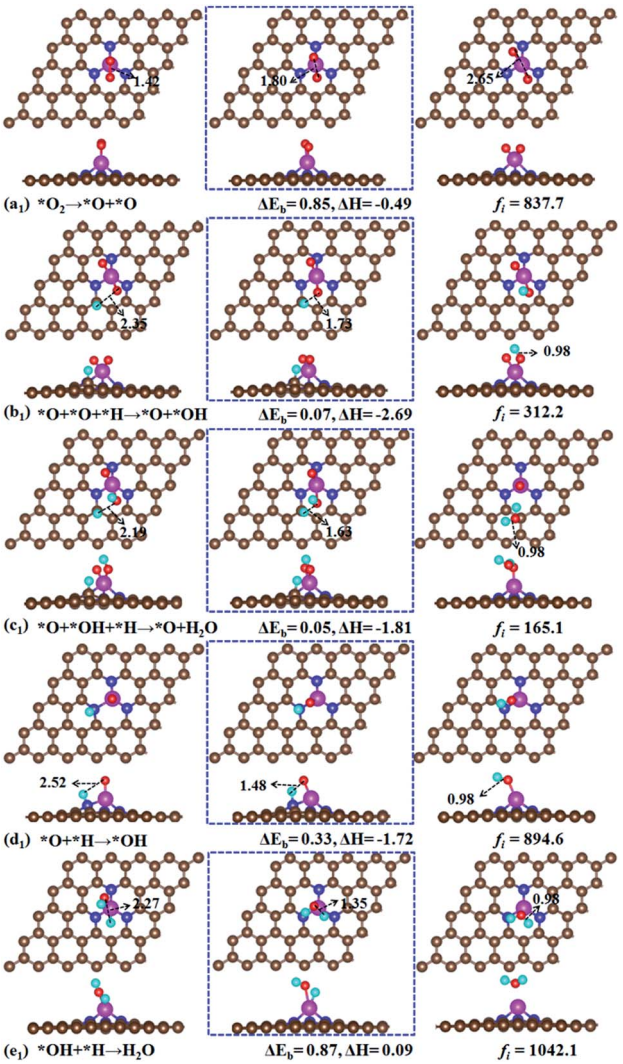

Fig. 5 Atomic structures of the initial state (left panel: IS), transition state (middle panel: TS), and final state (right panel: FS) for O_2 dissociation (a_1), atomic O hydrogenation (b_1), first H_2O formation (c_1), OH formation (d_1) and second H_2O formation (e_1). ΔE_b is the energy barrier (eV) and ΔH is the reaction energy (eV). f_i is the imaginary frequency for the transition state [cm^{-1}].

the second H_2O (Fig. 5). For the $O + H \rightarrow OH$ reaction, H atom would adsorb on either top C site or top N site, because the total energy of the two adsorbed system is nearly the same. For H atom adsorbed at top C site, the reaction needs to overcome an energy barrier of 1.09 eV (Fig. S2†), while the energy barrier is only 0.33 eV for H atom adsorbed on the top N site. This means that the hydrogenation of O atom with H adsorbed at top N site is kinetically favorable. This result also suggests that the reaction process depends strongly on the location of the introduced H atom. For the last hydrogenation step of OH, the OH and H co-adsorbed at top Fe site is energetically more favorable than H adsorbed at top C or top N site. The formation of second H_2O has an energy barrier of 0.87 eV with a slight endothermic reaction energy of 0.09 eV. If H atom first adsorbs at top C or N site, our calculation indicates H atom will first bond with Fe atom, then start the reaction with OH to form the second H_2O.

O_2 hydrogenation. For side-on O_2 configuration, our calculations show that the hydrogenation of O_2 molecule gives O + OH. That is, O–O bond is broken and OOH species is not formed. For end-on O_2 configuration, OOH species can be formed (Fig. 6f_1). For the $O_2 + H \rightarrow OOH$ reaction, it has a small energy barrier of 0.07 eV and a large exothermic reaction energy of −1.56 eV. The results suggest that O_2 hydrogenation to form OOH species is very easy. Following the OOH formation, there are two possible pathways, that is, OOH direct dissociation into O + OH and OOH hydrogenation into O + H_2O or OH + OH.

OOH dissociation – pathway II. For $OOH \rightarrow O + OH$ reaction, the OOH is spontaneously dissociated into O + OH without any barrier and large reaction energy of −2.10 eV. This is different from Fe–N_4 doped graphene, in which OOH dissociation needs to overcome an energy barriers of 0.56 eV (ref. 20) and 1.18 eV.[19] Following the formation of co-adsorbed O + OH, the further hydrogenation would give either O + H_2O or OH + OH. The former reaction has been already discussed in O_2 dissociation section (pathway I in Fig. 4). Therefore, we only discuss the later reaction in the following. For $O + OH + H \rightarrow OH + OH$ reaction, this process needs an energy barrier of 0.12 eV and is exothermic by −2.36 eV (Fig. 6g_1). The following hydrogenation reaction $OH + OH + H \rightarrow OH + H_2O$ has an energy barrier of 0.14 eV and a reaction energy of −1.28 eV (Fig. 5h_1). After the generated H_2O is desorbed from the Fe–N_3-Gra surface, the remaining OH at top Fe site would be hydrogenated to give the second H_2O (OH + H → H_2O in Fig. 5e_1), as also shown in pathway I, Fig. 4. After the release of the second H_2O molecule, the catalyst will be refreshed and a new cycle begins.

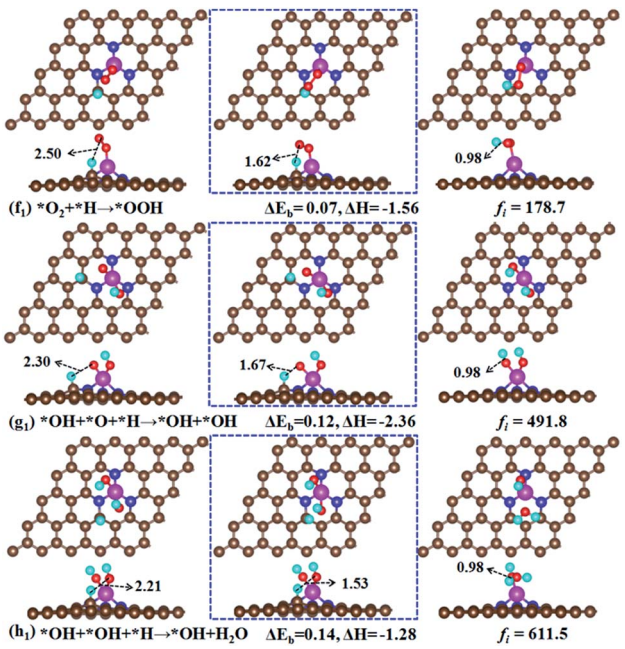

Fig. 6 Atomic structures of the initial state (left panel: IS), transition state (middle panel: TS), and final state (right panel: FS) for O_2 hydrogenation to OOH (f_1), the second OH formation (g_1), OH hydrogenation to H_2O (h_1). ΔE_b is the energy barrier (eV) and ΔH is the reaction energy (eV). f_i is the imaginary frequency for the transition state [cm^{-1}].

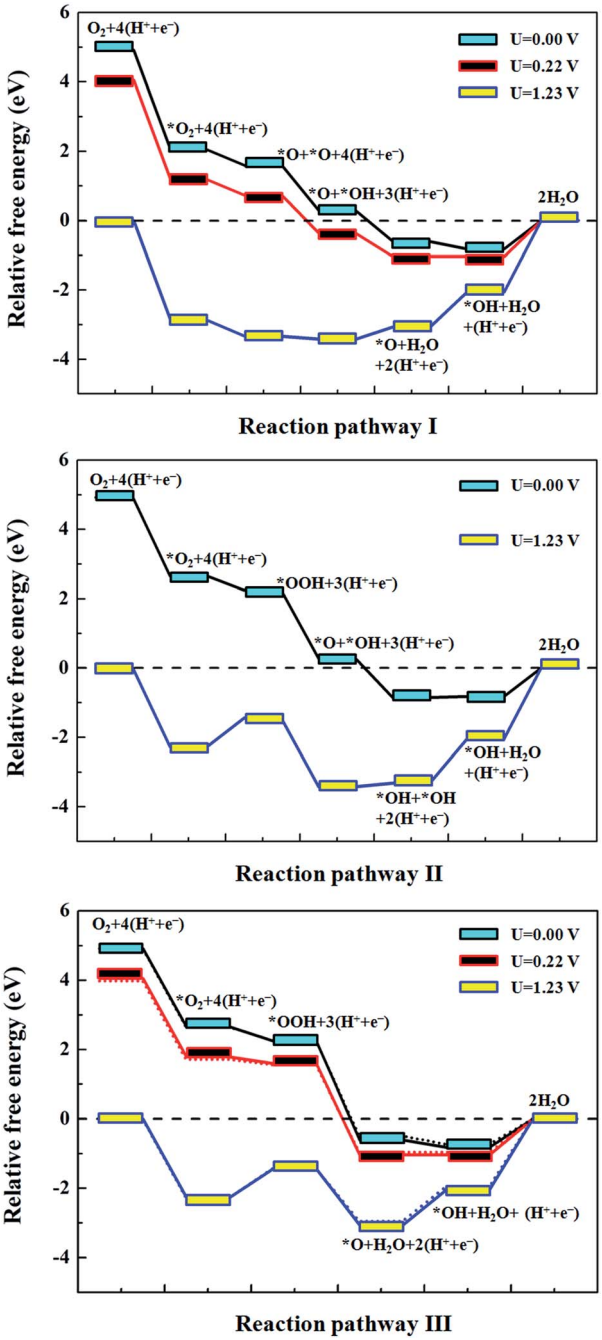

Fig. 7 The free energy diagrams for the reduction of O_2 to H_2O at different electrode potentials *U*. pathway I, O_2 dissociation; pathway II, OOH dissociation and pathway III, OOH hydrogenation; see also Fig. 4 for the detailed reaction pathways. The dotted lines in the bottom panel denote the results from the solvent environment.

OOH hydrogenation – pathway III. The hydrogenation of OOH would give HOOH, OH + OH and O + H_2O. As mentioned above, HOOH is very unstable and it dissociates into either OH + OH or O + H_2O. Meanwhile, our efforts to locate OH + OH from the direct hydrogenation of OOH also failed during the geometry optimizations. Therefore, only O + H_2O is observed. This is a spontaneous process and has more exothermic energy of

−3.59 eV. The remaining O at top Fe site will proceed directly with the two sequential hydrogenation processes to form the second H_2O (O + H → OH and OH + H → H_2O in pathway I, Fig. 4).

In a word, the four-electron ORR on the Fe–N_3-Gra surface could proceed through three possible reaction pathways (Fig. 4). The rate-determining step in the three possible pathways is the formation of the second H_2O, *i.e.*, OH + H → H_2O. The energy barrier of 0.87 eV, smaller than 0.56 eV (ref. 20) and 0.62 eV (ref. 19) for Fe–N_4 doped graphene, but close to 0.80 eV for pure Pt(111).[53] For Fe–N_4-Gra, the two-electron ORR is observed because HOOH species could be stably adsorbed on catalyst surface.[19] However, the HOOH species will be decomposed immediately on Fe–N_3-Gra surface, suggesting a four-electron pathway. This suggests that the Fe–N_3-Gra could be a high performance catalyst for ORR. The obtained three pathways are competitive for the most favorable pathway, with the pathway of O_2 hydrogenation being slightly favored.

3.4 Effect of electrode potentials on the ORR

Since all of the above results are obtained under zero electrode potential, while in reality, electrochemical ORR at the electrode occurs under positive potentials, we studied the effect of the electrode potentials on the free energy of ORR on Fe–N_3-Gra. The free energy diagrams for three possible pathways are given in Fig. 7 based on the method of Nørskov *et al.*[48] For the three pathways, all of the reduction steps except the OH reduction to H_2O are downhill at zero potential. The endothermic process for the second H_2O formation is due to the strong adsorption of OH (−4.35 eV, Table 2) on the catalyst surface. For pathways I and III, the another step, *i.e.*, O + H_2O + H → OH + H_2O becomes uphill at potential larger than 0.22 V. A similar trend is observed after the solvent effect is considered (Fig. 7, dotted lines in the bottom panel).

4. Conclusions

Fe–N_3 doped graphene (Fe–N_3-Gra) is energetically stable. Fe–N_3 moiety and its six adjacent C atoms are the catalytic active sites for the oxygen reduction reaction on the catalyst surface. Both DFT and molecular dynamics studies indicate that HOOH does not exist on the catalyst surface, implying the direct four-electron process for Fe–N_3-Gra. O_2 dissociation and O_2 hydrogenation are competitive for the most favorable pathway, in which the pathway of O_2 hydrogenation is slightly favored. For these pathways, the rate-determining step is the formation of the second H_2O, *i.e.*, OH + H → H_2O, with an energy barrier of 0.87 eV. Due to the strong adsorption of OH on the catalyst surface, the endothermic process is observed for the second H_2O formation at zero potential.

Acknowledgements

This work is supported by the National Natural Science Foundation of China (21503210, 21673220, 21261013), Jilin Province Natural Science Foundation (20150101012JC), the Program for Young Talents of Science and Technology in Universities of Inner Mongolia Autonomous Region (NJYT-15-B16), the Program for Innovative Research Team in Universities of Inner Mongolia Autonomous Region (NMGIRT-A1603), the Natural Science Foundation of Inner Mongolia Autonomous Region (Grant No. 2015MS0120 and 2011BS0104), and the Key Science Research Project of Inner Mongolia University of Technology (Grant No. ZD201517 and ZD201117). The computing time is supported by the High Performance Computing Center of Jilin University, Changchun Normal University, and Jilin Province Supercomputing Center.

References

1 B. C. H. Steele and A. Heinzel, *Nature*, 2001, **414**, 345–352.
2 X. Xu, T. Yuan, Y. K. Zhou, Y. W. Li, J. M. Lu, X. H. Tian, D. L. Wang and J. Wang, *Int. J. Hydrogen Energy*, 2014, **39**, 16043–16052.
3 J. Snyder, T. Fujita, M. W. Chen and J. Erlebacher, *Nat. Mater.*, 2010, **9**, 904–907.
4 Y. J. Wang, N. N. Zhao, B. Z. Fang, H. Li, X. T. T. Bi and H. J. Wang, *Chem. Rev.*, 2015, **115**, 3433–3467.
5 B. Fang, J. H. Kim, M. S. Kim and J. S. Yu, *Acc. Chem. Res.*, 2013, **46**, 1397–1406.
6 B. Fang, N. K. Chaudhari, M. S. Kim, J. H. Kim and J. S. Yu, *J. Am. Chem. Soc.*, 2009, **131**, 15330–15338.
7 M. K. Debe, *Nature*, 2012, **486**, 43–51.
8 R. Jasinski, *Nature*, 1964, **201**, 1212–1213.
9 G. Wu, K. L. More, C. M. Johnston and P. Zelenay, *Science*, 2011, **332**, 443–447.
10 M. Lefevre, E. Proietti, F. Jaouen and J. P. Dodelet, *Science*, 2009, **324**, 71–74.
11 A. Serov, K. Artyushkova and P. Atanassov, *Adv. Energy Mater.*, 2014, **4**, 919–926.
12 K. Artyushkova, A. Serov, S. Rojas-Carbonell and P. Atanassov, *J. Phys. Chem. C*, 2015, **119**, 25917–25928.
13 S. Jiang, C. Z. Zhu and S. J. Dong, *J. Mater. Chem. A*, 2013, **1**, 3593–3599.
14 Q. Liu and J. Y. Zhang, *Langmuir*, 2013, **29**, 3821–3828.
15 S. H. Liu, Y. F. Dong, Z. Y. Wang, H. W. Huang, Z. B. Zhao and J. S. Qiu, *J. Mater. Chem. A*, 2015, **3**, 19657–19661.
16 L. L. Zhang, A. Q. Wang, W. T. Wang, Y. Q. Huang, X. Y. Liu, S. Miao, J. Y. Liu and T. Zhang, *ACS Catal.*, 2015, **5**, 6563–6572.
17 J. Kang, H. Wang, S. Ji, J. Key and R. F. Wang, *J. Power Sources*, 2014, **251**, 363–369.
18 J. Liang, R. F. Zhou, X. M. Chen, Y. H. Tang and S. Z. Qiao, *Adv. Mater.*, 2014, **26**, 6074–6079.
19 J. Zhang, Z. J. Wang and Z. P. Zhu, *J. Power Sources*, 2014, **255**, 65–69.
20 S. Kattel and G. F. Wang, *J. Phys. Chem. Lett.*, 2014, **5**, 452–456.
21 X. L. Zhang, Z. S. Lu and Z. X. Yang, *Int. J. Hydrogen Energy*, 2016, **41**, 21212–21220.
22 S. Kattel, P. Atanassov and B. Kiefer, *Phys. Chem. Chem. Phys.*, 2013, **15**, 148–153.
23 Z. Lu, G. Xu, C. He, T. Wang, L. Yang, Z. Yang and D. Ma, *Carbon*, 2015, **84**, 500–508.

24 J. B. Yang, D. J. Liu, N. N. Kariuki and L. X. Chen, *Chem. Commun.*, 2008, **3**, 329–331.
25 A. G. Kong, X. F. Zhu, Z. Han, Y. Y. Yu, Y. B. Zhang, B. Dong and Y. K. Shan, *ACS Catal.*, 2014, **4**, 1793–1800.
26 Y. S. Zhu, B. S. Zhang, X. Liu, D. W. Wang and D. S. Su, *Angew. Chem., Int. Ed.*, 2014, **53**, 10673–10677.
27 F. P. Pan, Q. P. Zhao, J. Wang and J. Y. Zhang, *ChemElectroChem*, 2015, **2**, 2032–2040.
28 H. He, Y. K. Lei, C. Xiao, D. R. Chu, R. R. Chen and G. F. Wang, *J. Phys. Chem. C*, 2012, **116**, 16038–16046.
29 E. F. Holby, G. Wu, P. Zelenay and C. D. Taylor, *J. Phys. Chem. C*, 2014, **118**, 14388–14393.
30 S. Kabir, K. Artyushkova, B. Kiefer and P. Atanassov, *Phys. Chem. Chem. Phys.*, 2015, **17**, 17785–17789.
31 J. Sun, Y. H. Fang and Z. P. Liu, *Phys. Chem. Chem. Phys.*, 2014, **16**, 13733–13740.
32 S. Kattel, P. Atanassov and B. Kiefer, *Phys. Chem. Chem. Phys.*, 2014, **16**, 13800–13806.
33 U. I. Koslowski, I. Abs-Wurmbach, S. Fiechter and P. Bogdanoff, *J. Phys. Chem. C*, 2008, **112**, 15356–15366.
34 D. H. Lee, W. J. Lee, W. J. Lee, S. O. Kim and Y. H. Kim, *Phys. Rev. Lett.*, 2011, **106**, 175502.
35 D. Deng, X. Chen, L. Yu, X. Wu, Q. Liu, Y. Liu, H. Yang, H. Tian, Y. Hu, P. Du, R. Si, J. Wang, X. Cui, H. Li, J. Xiao, T. Xu, J. Deng, F. Yang, P. N. Duchesne, P. Zhang, J. Zhou, L. Sun, J. Li, X. Pan and X. Bao, *Sci. Adv.*, 2015, **1**, 1500462.
36 H. R. Byon, J. Suntivich and Y. Shao-Horn, *Chem. Mater.*, 2011, **23**, 3421–3428.
37 S. Kattel, P. Atanassov and B. Kiefer, *J. Phys. Chem. C*, 2012, **116**, 8161–8166.
38 P. Hohenberg and W. Kohn, *Phys. Rev. [Sect.] A*, 1964, **136**, 864–871.
39 W. Kohn and L. J. Sham, *Phys. Rev. [Sect.] A*, 1965, **140**, 1133–1138.
40 G. Kresse and J. Furthmuller, *Phys. Rev. B: Condens. Matter Mater. Phys.*, 1996, **54**, 11169–11186.
41 G. Kresse and J. Furthmuller, *Phys. Rev. B: Condens. Matter Mater. Phys.*, 1996, **6**, 15–50.
42 P. E. Blochl, *Phys. Rev. B: Condens. Matter Mater. Phys.*, 1994, **50**, 17953–17979.
43 J. P. Perdew, K. Burke and M. Ernzerhof, *Phys. Rev. Lett.*, 1996, **77**, 3865–3868.
44 H. J. Monkhorst and J. D. Pack, *Phys. Rev. B: Solid State*, 1976, **13**, 5188–5192.
45 G. Henkelman, B. P. Uberuaga and H. Jonsson, *J. Chem. Phys.*, 2000, **113**, 9901–9904.
46 S. Grimme, *J. Comput. Chem.*, 2006, **27**, 1787–1799.
47 S. Grimme, J. Antony, S. Ehrlich and H. Krieg, *J. Chem. Phys.*, 2010, **132**, 154104.
48 J. K. Norskov, J. Rossmeisl, A. Logadottir, L. Lindqvist, J. R. Kitchin, T. Bligaard and H. Jonsson, *J. Phys. Chem. B*, 2004, **108**, 17886–17892.
49 K. T. Chan, J. B. Neaton and M. L. Cohen, *Phys. Rev. B: Solid State*, 2008, **77**, 235430.
50 P. Zhang, X. F. Chen, J. S. Lian and Q. Jiang, *J. Phys. Chem. C*, 2012, **116**, 17572–17579.
51 R. R. Chen, H. X. Li, D. Chu and G. F. Wang, *J. Phys. Chem. C*, 2009, **113**, 20689–20697.
52 K. Li, Y. Li, Y. Wang, F. He, M. G. Jiao, H. Tang and Z. J. Wu, *J. Mater. Chem. A*, 2015, **3**, 11444–11452.
53 Z. Y. Duan and G. F. Wang, *Phys. Chem. Chem. Phys.*, 2011, **13**, 20178–20187.